

Dynamical Tides in Highly Eccentric Binaries: Chaos, Dissipation and Quasi-Steady State

Michelle Vick, Dong Lai*

Cornell Center for Astrophysics and Planetary Science, Department of Astronomy,
Cornell University, Ithaca, NY 14853, USA

*To whom correspondence should be addressed; E-mail: dong@astro.cornell.edu.

Highly eccentric binary systems appear in many astrophysical contexts, ranging from tidal capture in dense star clusters, precursors of stellar disruption by massive black holes, to high-eccentricity migration of giant planets. In a highly eccentric binary, the tidal potential of one body can excite oscillatory modes in the other during a pericenter passage, resulting in energy exchange between the modes and the binary orbit. These modes exhibit one of three behaviors over multiple passages: low-amplitude oscillations, large amplitude oscillations corresponding to a resonance between the orbital frequency and the mode frequency, and chaotic growth. We study these phenomena with an iterative map, fully exploring how the mode evolution depends on the pericenter distance and other parameters. In addition, we show that the dissipation of mode energy results in a quasi-steady state, with gradual orbital decay punctuated by resonances, even in systems where the mode amplitude would initially grow stochastically. A newly captured star around a black hole can experience significant orbital decay and heating due to the chaotic growth of the mode amplitude and dissipation. A giant planet pushed into a high-eccentricity orbit may experience a similar effect and become a warm Jupiter.

Introduction Highly eccentric binaries appear in a variety of astrophysical contexts. In dense stellar clusters, two stars can be captured into a bound orbit with each other if a close encounter transfers enough energy into stellar oscillations (1–3). Such tidally captured binaries are highly eccentric and often involve compact objects (black holes and neutron stars). Massive black holes in nuclear star clusters may tidally capture normal stars, and could build up significant masses through successive captures (4). Indeed, stars on highly eccentric orbits around massive black holes could be precursors of tidal disruption events (5), dozens of which have already been observed, e.g. (6, 7). Heating from tidal dissipation may affect the structure of stars moving toward disruption, potentially alter the observational signal of these events (8, 9). In exoplanetary systems, hot and warm Jupiters may be formed through high-eccentricity migration, in which a

giant planet is pushed into a highly eccentric orbit by the gravitational perturbation from a distant companion (a star or planet); at periastron, tidal dissipation in the planet reduces the orbital energy, leading to inward migration and circularization of the planet’s orbit (10–15). Finally, the *Kepler* spacecraft has revealed a class of high-eccentricity stellar binaries with short orbital periods, whose light curves are shaped by tidal distortion and reflection at periastron (16–18); many of these “heartbeat stars” also exhibit signatures of tidally induced stellar oscillations (19–22).

In a highly eccentric binary, dynamical tidal interaction occurs mainly near pericenter and manifests as repeated tidal excitations of stellar oscillation modes. Since tidal excitation depends on the oscillation phase, the magnitude and direction of the energy transfer between the orbit and the modes may vary from one pericenter passage to the next. Earlier works in the context of tidal-capture binaries (23) have suggested that for some combinations of orbital parameters, the energy in stellar modes may behave chaotically and grow to very large values. The possibility of chaotic growth of mode energy was also explored in (24) in the context of giant planets on eccentric orbits. On the other hand, it is also expected that the long-term evolution of the binary depends on how effectively the binary components can dissipate energy (25, 26). Indeed, in the presence of dissipation, the system may reach a quasi-steady state in which the orbit-averaged mode energy remains constant (20, 27, 28). How such a quasi-steady state may emerge (if at all) from a possibly chaotic dynamical system is unclear.

Given the important role played by dynamical tides in various eccentric stellar/planetary binary systems, a clear understanding of the dynamics of repeated tidal excitations of oscillation modes and the related tidal dissipation is desirable. In this paper, we develop an iterative map that accurately captures the dynamics and dissipation of the coupled “eccentric orbit + oscillation modes” system. Using this map, we aim to (i) characterize the classes of behavior exhibited by eccentric binaries due to dynamical tides, (ii) explore the orbital parameters that lead to these behaviors, and (iii) study how the inclusion of mode damping affects the evolution of the system. The results of this study are applicable to the large variety of systems mentioned above.

Iterative Map for Mode Amplitudes Consider a binary system consisting of a primary body M (a star or planet) on an eccentric orbit with a companion M' (treated as a point mass). Near pericenter, the tidal force from M' excites oscillations in M . When the oscillation amplitudes are sufficiently small, we can follow the evolution of the modes and the orbit using linear hydrodynamics. For highly eccentric orbits ($1 - e \ll 1$), the orbital trajectory around the pericenter remains almost unchanged even for large changes in the binary semi-major axis. Under these conditions, the full hydrodynamical solution of the system can be reduced to an iterative map (see Appendix A). We present the following map for a single-mode system and will discuss later the effects of multiple modes.

We define the dimensionless mode energy and binary orbital energy in units of $|E_{B,0}|$ (the initial binary orbital energy), i.e., $\tilde{E} = E/|E_{B,0}|$. Consider a single mode of the star with frequency ω and (linear) damping rate γ . Let a_{k-1} be the mode amplitude just before the k -th pericenter passage. Immediately after the k -th passage, the mode amplitude becomes

$$a_{k-} = a_{k-1} + \Delta a, \quad (1)$$

where Δa (real) is the mode amplitude change in the “first” passage (i.e., when there is no pre-existing oscillation). We normalize a_k such that the (dimensionless) mode energy just after k -th passage is $\tilde{E}_{k-} = |a_{k-}|^2$. Thus the energy transfer to the mode in the k -th passage is

$$\Delta \tilde{E}_k = |a_{k-}|^2 - |a_{k-1}|^2 = |a_{k-1} + \Delta a|^2 - |a_{k-1}|^2. \quad (2)$$

The binary orbital energy ($\tilde{E}_{B,k}$) immediately after the k -th passage is given by

$$\tilde{E}_{B,k} = \tilde{E}_{B,k-1} - \Delta\tilde{E}_k = \tilde{E}_{B,0} - \sum_{j=1}^k \Delta\tilde{E}_j, \quad (3)$$

and the corresponding orbital period is

$$\frac{P_k}{P_0} = \left(\frac{\tilde{E}_{B,0}}{\tilde{E}_{B,k}} \right)^{3/2}, \quad (4)$$

where $\tilde{E}_{B,0} = -1$. The mode amplitude just before the $(k+1)$ -th passage is

$$a_k = a_{k-} e^{-(i\omega+\gamma)P_k} = (a_{k-1} + \Delta a) e^{-(i+\hat{\gamma})\hat{P}_k}, \quad (5)$$

where we have defined the dimensionless damping rate and orbital period

$$\hat{\gamma} = \frac{\gamma}{\omega}, \quad \hat{P}_k = \omega P_k. \quad (6)$$

Equations (1)-(5) complete the map from one orbit to the next, starting from the initial condition $a_0 = 0$, $\tilde{E}_0 = 0$, $\tilde{E}_{B,0} = -1$. The map depends on three parameters:

$$\hat{P}_0 \equiv \omega P_0, \quad (7)$$

$$|\Delta\hat{P}_1| \equiv \omega |\Delta P_1| \simeq \frac{3}{2} \hat{P}_0 (\Delta a)^2, \quad (8)$$

$$\hat{\gamma} = \frac{\gamma}{\omega} = \frac{\gamma P_0}{\hat{P}_0} = \frac{1}{\hat{P}_0} \left(\frac{P_0}{t_{\text{damp}}} \right). \quad (9)$$

To relate \hat{P}_0 and $|\Delta\hat{P}_1|$ to the physical parameters of the system, we scale the mode frequency ω to $\Omega_{\text{peri}} \equiv (GM_t/r_{\text{peri}}^3)^{1/2}$ (where $M_t = M + M'$, and r_{peri} is the pericenter distance), and find

$$\hat{P}_0 = \frac{2\pi(\omega/\Omega_{\text{peri}})}{(1-e)^{3/2}}. \quad (10)$$

The parameter $|\Delta\hat{P}_1|$ is related to the energy transfer in the ‘‘first’’ pericenter passage via $|\Delta\hat{P}_1|/\hat{P}_0 = (3/2)|\Delta E_1/E_{B,0}|$. If we scale the r_{peri} by the tidal radius $r_{\text{tide}} = R(M_t/M)^{1/3}$ (where R is the stellar radius), i.e., $\eta = r_{\text{peri}}/r_{\text{tide}}$, we have

$$\Delta E_1 = -\frac{GM'^2 R^5}{r_{\text{peri}}^6} T(\eta, \omega/\Omega_{\text{peri}}), \quad (11)$$

where T is a dimensionless function of η and $\omega/\Omega_{\text{peri}}$. Then,

$$|\Delta\hat{P}_1| = \frac{6\pi(\omega/\Omega_{\text{peri}})}{(1-e)^{5/2}} \left(\frac{M'}{M} \right) \left(\frac{M}{M_t} \right)^{5/3} \eta^{-5} T(\eta, \omega/\Omega_{\text{peri}}). \quad (12)$$

In general, $|\Delta\hat{P}_1|$ falls off steeply with η . However, even when η is large (weak tidal encounter), $|\Delta\hat{P}_1|$ can be significant for highly eccentric systems (with $1 - e \ll 1$).

The map (1)-(5) assumes that (i) energy transfer occurs instantaneously at pericenter; (ii) at each pericenter passage, the change in mode amplitude, $a_{k-} - a_{k-1}$, is the same; and (iii) the mode energy is always much less than the binding energy of the star. The first condition is satisfied when $1 - e \ll 1$. The second condition requires that the pericenter distance remains constant, which in turn requires that the fractional change in orbital angular momentum, $\Delta L/L$, remain small throughout orbital evolution. Using $\Delta L \sim \Delta E_B/\Omega_{\text{peri}}$ as an estimate, we find that the condition $\Delta L/L \ll 1$ becomes

$$\frac{\Delta L}{L} \sim \frac{1}{2\sqrt{2}} \Delta\tilde{E}_B(1 - e) \ll 1. \quad (13)$$

Thus, for sufficiently eccentric orbits, r_{peri} is roughly constant even when the orbital energy changes by $\Delta\tilde{E}_B \sim 10$. The third condition, $E_k \ll GM^2/R$, yields the expression

$$\frac{\tilde{E}_k(1 - e)}{2\eta} \left(\frac{M'}{M}\right) \left(\frac{M_t}{M}\right)^{-1/3} \ll 1. \quad (14)$$

Again, this is easiest to satisfy for very eccentric orbits.

Mode Energy Evolution without Dissipation We first study the dynamics of the “eccentric orbit + mode” system without dissipation ($\hat{\gamma} = 0$). The iterative map described in Eqs. 1-5 displays a variety of behaviors depending on \hat{P}_0 and $|\Delta\hat{P}_1|$. We can gain insight into the evolution of the system by recording \tilde{E}_{max} , the maximum mode energy reached over many orbits; this quantity reveals whether energy transfer to stellar modes is relatively small or whether the orbit can change substantially by transferring large amounts of energy. Figure 1 shows \tilde{E}_{max} after 10^4 orbits for systems with a range of \hat{P}_0 and $|\Delta\hat{P}_1|$.

The system evolution has a complex dependence on \hat{P}_0 and $|\Delta\hat{P}_1|$. In general, the mode energy exhibits oscillatory behavior for small $|\Delta\hat{P}_1|$ and chaotic growth for large $|\Delta\hat{P}_1|$. However, Fig. 1 shows exceptions to this trend. The figure also suggests that the response to \hat{P}_0 is periodic and the mode amplitude is larger in magnitude near resonances where the orbital frequency is commensurate with the mode frequency. The map displays three primary types of behaviors — low-amplitude oscillation, resonant oscillation, and chaotic evolution. Transitions between the three regimes are complicated. However, within each regime, \tilde{E}_{max} exhibits simple dependence on \hat{P}_0 and $|\Delta\hat{P}_1|$.

Oscillatory Behaviour When $|\Delta\hat{P}_1|/(2\pi) \lesssim 0.05$ and $\tilde{P}_0/(2\pi)$ is not close to an integer, the mode exhibits low-amplitude oscillations, shown in the top panels of Fig. 2. In this regime, the orbital period is nearly constant ($\hat{P}_k \simeq \hat{P}_0$), and the map from Eqs. 1-5 can be written simply as

$$a_k \simeq (a_{k-1} + \Delta a) e^{-i\hat{P}_0}. \quad (15)$$

This can be solved with the initial condition $a_0 = 0$, yielding

$$a_k \simeq \frac{\Delta a}{e^{i\hat{P}_0} - 1} \left(1 - e^{-i\hat{P}_0 k}\right). \quad (16)$$

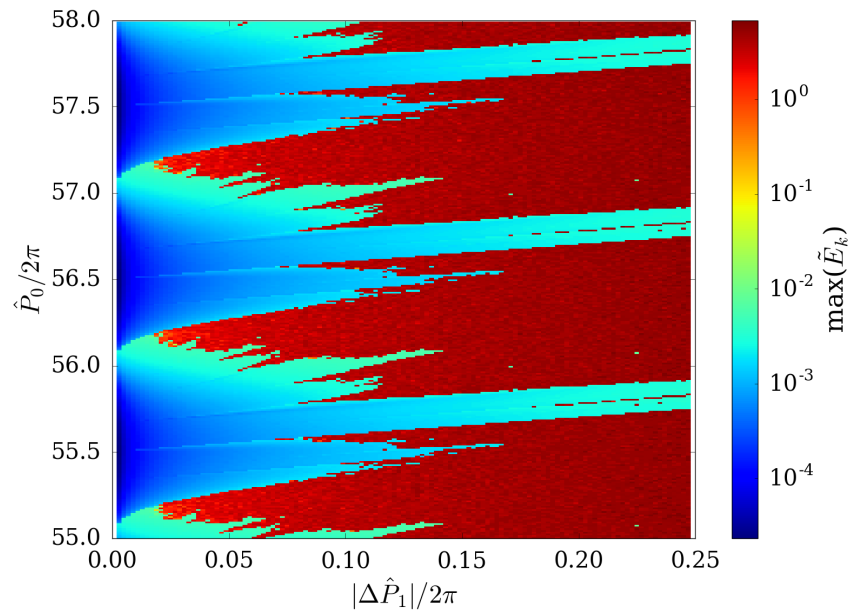


Figure 1: The maximum mode energy reached in 10^4 orbits as a function of $|\Delta \hat{P}_1|/2\pi$ and $\hat{P}_0/2\pi$. The energy is normalized to the initial orbital energy of the binary. In the dark blue regions, the mode exhibits low-energy oscillations. In the light green regions, the mode exhibits high-amplitude oscillations corresponding to a resonance. The red regions indicate chaotic mode evolution.

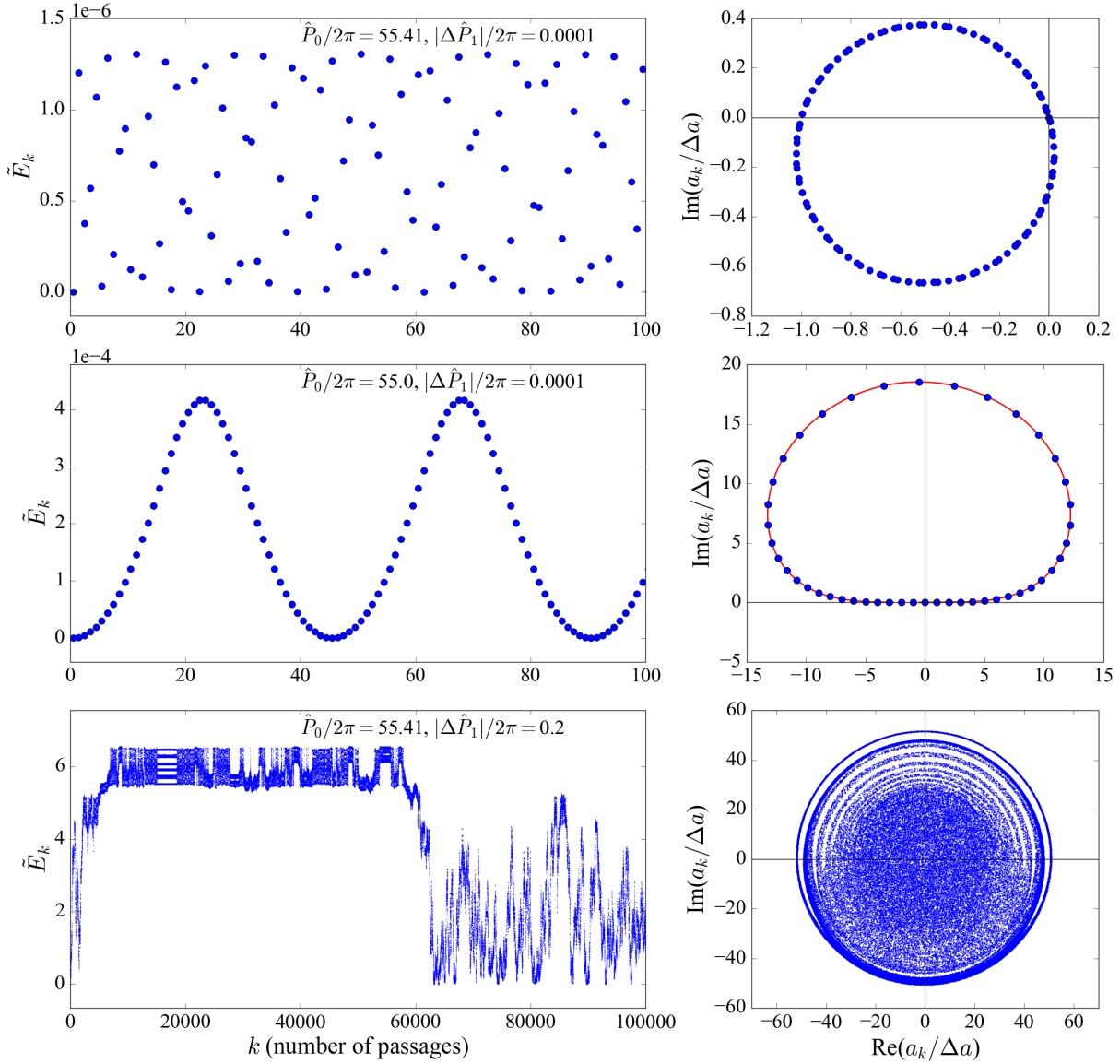


Figure 2: Left Column: The evolution of the mode energy over multiple pericenter passages. Right Column: The complex mode amplitude a_k (normalized to Δa , the change in mode amplitude during the first pericenter passage). From top to bottom, the three rows correspond to different types of behaviors — low-amplitude oscillations, resonant behavior, and chaotic evolution. The red line is from Eq. 56 in Appendix B.1.

Note that, in the complex plane, this solution has the form of a circle of radius $|1/(e^{i\hat{P}_0} - 1)|$ centered on $1/(e^{i\hat{P}_0} - 1)$, as shown in Fig. 2 [a result previously seen in (24)]. From Eq. 16, the maximum mode energy in this regime is

$$\tilde{E}_{\max} \simeq \frac{2(\Delta a)^2}{1 - \cos \hat{P}_0}. \quad (17)$$

This result demonstrates that our assumption of $\hat{P}_k \simeq \hat{P}_0$ performs well when $(\Delta a)^2 \ll 1$ and \hat{P}_0 is not too close to an integer multiple of 2π . Under these conditions, the mode energy remains of order $(\Delta a)^2 = \Delta \tilde{E}_1$, the energy transfer in the “first” pericenter passage.

Resonance Figure 1 indicates that the stellar mode exhibits large-amplitude oscillations for $\hat{P}_0 \simeq 2\pi N$ (with $N = \text{integer}$), i.e., when the orbital period P_0 is nearly an integer multiple of the mode period $2\pi/\omega$. To understand this behavior, we assume $\tilde{E}_k = |a_k|^2 \ll 1$, which holds true in the non-chaotic regime. With no dissipation, equation (4) is replaced by

$$\hat{P}_k \simeq \hat{P}_0 \left(1 - \frac{3}{2}|a_{k-}|^2 \right) = \hat{P}_0 - |\Delta \hat{P}_1| |z_k|^2, \quad (18)$$

where we have defined $z_k \equiv a_{k-}/\Delta a$ and used Eq. 8. The map can then be written as

$$z_{k+1} = 1 + z_k e^{-i\hat{P}_k} \simeq 1 + z_k e^{-i\hat{P}_0 + i|\Delta \hat{P}_1| |z_k|^2}. \quad (19)$$

Near a resonance, with $|\delta \hat{P}_0| = |\hat{P}_0 - 2\pi N| \ll 1$, the above map can be further simplified to $z_{k+1} - z_k \simeq 1 + z_k(-i\delta \hat{P}_0 + i|\Delta \hat{P}_1| |z_k|^2)$. The maximum mode amplitude near resonance is determined by setting the nonlinear term $|\Delta \hat{P}_1| |z_k|^3 \sim 1$, giving $|z_{\text{res}}| \sim |\Delta \hat{P}_1|^{-1/3}$. The corresponding mode energy is

$$\tilde{E}_{\text{res}} \sim \frac{(\Delta a)^2}{|\Delta \hat{P}_1|^{2/3}} \sim \frac{|\Delta \hat{P}_1|^{1/3}}{\hat{P}_0}. \quad (20)$$

Equation (20) is valid for $|\delta \hat{P}_0| \lesssim |\Delta \hat{P}_1|^{1/3}$, and agrees with our numerical result (see Appendix B.1 for more details).

Chaotic Growth Chaotic growth of mode energy typically occurs when $|\Delta \hat{P}_1| \gtrsim 1$, i.e., when enough energy is transferred in a pericenter passage to change the orbital period and cause appreciable phase shift of the mode. In this regime, the mode amplitude fills a circle in the complex plane after the binary evolves for many orbits, as shown in the bottom panels of Fig. 2. We can verify the chaotic nature of this behavior through a Lyapunov analysis; we find that the Lyapunov time is about an orbital period (see Appendix B.3).

In the absence of dissipation, the mode amplitude map is simply

$$a_k = (a_{k-1} + \Delta a) e^{-i\hat{P}_k}, \quad \text{with } \hat{P}_k = \hat{P}_0 (1 + |a_k|^2)^{-3/2}. \quad (21)$$

When the change in orbital period between pericenter passages, $\Delta\hat{P}_k = \hat{P}_k - \hat{P}_{k-1}$, is much larger than unity, \hat{P}_k approximately takes on random phases. This random-phase model captures the key features of mode growth in the chaotic regime (see Fig. 8 in Appendix B.4). The mode energy after the k -th passages can be written as

$$\tilde{E}_k = \sum_{j=1}^k \Delta\tilde{E}_j = \sum_{j=1}^k [(\Delta a)^2 + 2(\Delta a)\text{Re}(a_{j-1})]. \quad (22)$$

If we *assume* that a_{j-1} exhibits random phases, then

$$\langle \tilde{E}_k \rangle \sim (\Delta a)^2 k, \quad (23)$$

[a result previously obtained in (23,24)], which provides a crude description of the chaotic mode growth, shown in Fig. 8.

Although \tilde{E}_{\max} can become very large, Fig. 2 suggests that the mode energy cannot exceed a maximum value, a feature not captured by the random-phase model. This can be understood from the fact that as the mode energy increases, the the range of possible $\Delta\hat{P}_k$ decreases. Indeed, from Eq. 21 we find

$$\Delta\hat{P}_k \equiv \hat{P}_k - \hat{P}_{k-1} \simeq -3\Delta a \hat{P}_0 \frac{\text{Re}(a_{k-1})}{(1 + |a_{k-1}|^2)^{5/2}}. \quad (24)$$

Setting $\Delta\hat{P}_k \sim 1$ leads to a maximum mode energy

$$\tilde{E}_{\max} = (|a_k|^2)_{\max} \sim (\hat{P}_0 \Delta a)^{1/2} \sim (|\Delta\hat{P}_1| \hat{P}_0)^{1/4}. \quad (25)$$

More discussion on the maximum mode energy in the chaotic regime can be found in Appendix B.4. Note that \tilde{E}_{\max} of order a few can be easily reached for a large range of \hat{P}_0 and $|\Delta\hat{P}_1|$ (see Fig. 2). Such a large mode energy implies order unity change in the semi-major axis of the orbit, but for $1 - e \ll 1$ it does not necessarily violate the requirements needed for the validity of the iterative map (see Eqs. 13-14).

Mode Energy Evolution with Dissipation We now consider the effect of dissipation on the evolution of the system. In the presence of mode damping ($\gamma \neq 0$), energy is preferentially transferred from the orbit to the stellar mode which then dissipates, causing long-term orbital decay. In the extreme case when the mode damping time $t_{\text{damp}} = \gamma^{-1}$ is shorter than the orbital period P , the energy transfer in each pericenter passage ΔE_1 is dissipated, and the orbital energy E_B simply decays according to

$$\frac{dE_B}{dt} \simeq -\frac{\Delta E_1}{P}, \quad (\text{for } t_{\text{damp}} \lesssim P). \quad (26)$$

Below, we will consider the more realistic situation of $t_{\text{damp}} \gg P$.

Quasi-Steady State Consider a system with $|\Delta\hat{P}_1| \ll 1$ and an orbital period that is far from resonance. The mode energy will stay around ΔE_1 , and can attain a quasi-steady state after a few damping times (see Fig. 3). Indeed, since the orbital period P remains roughly constant over multiple damping times, the map simplifies to

$$a_k \simeq (a_{k-1} + \Delta a) e^{-(i+\hat{\gamma})\hat{P}}. \quad (27)$$

Assuming $a_0 = 0$, we find

$$a_k \simeq \frac{\Delta a}{e^{(i+\hat{\gamma})\hat{P}} - 1} \left[1 - e^{-(i+\hat{\gamma})\hat{P}k} \right]. \quad (28)$$

Clearly, the mode amplitude approaches a constant value after a few damping times ($kP \gg \gamma^{-1}$), and the mode energy reaches the steady-state value (28):

$$\tilde{E}_{ss} \simeq \frac{\Delta\tilde{E}_1 e^{-\hat{\gamma}\hat{P}}}{2(\cosh \hat{\gamma}\hat{P} - \cos \hat{P})} \simeq \frac{\Delta\tilde{E}_1}{4 \sin^2(\hat{P}/2) + (\hat{\gamma}\hat{P})^2}, \quad (29)$$

where the second equality assumes $\hat{\gamma}\hat{P} = \gamma P \ll 1$, or $t_{\text{damp}} \gg P$. The steady-state energy is of order $\Delta\tilde{E}_1$, provided that the system is not near a resonance. In the steady state, the star dissipates all the “additional” energy gained at each pericenter passage, and thus the orbital energy decays according to

$$\frac{d\tilde{E}_B}{dt} \simeq -2\gamma\tilde{E}_{ss} \quad \text{or} \quad \frac{dE_B}{dt} \simeq -\frac{2E_{ss}}{t_{\text{damp}}}, \quad (\text{for } t_{\text{damp}} \gg P). \quad (30)$$

Passing Through Resonances As the binary orbit experiences quasi-steady decay, it will encounter resonances with the stellar mode ($\hat{P}/2\pi = \text{integer}$), during which rapid orbital decay occurs (see Fig. 4).

The change in orbital energy when a system moves through a resonance depends on how the resonance time t_{res} (the timescale for the mode energy of a system near resonance to reach \tilde{E}_{res}) compares with t_{damp} . In most likely situations, the resonance time $t_{\text{res}} \sim P/|\Delta\hat{P}_1|^{1/3}$ (see Appendix B.2) is much shorter than t_{damp} , so the orbital energy is quickly transferred to the stellar mode as the system approaches the resonance, and the mode energy reaches the maximum resonance value given by Eq. 20. All of this energy is dissipated within a few t_{damp} , resulting in a net change in the orbital energy during the resonance $\Delta\tilde{E}_{B,\text{res}} \simeq \tilde{E}_{\text{res}} \sim |\Delta\hat{P}_1|^{1/3}/\hat{P}$. By comparison, the quasi-steady orbital energy change between adjacent resonances [from $\hat{P} = 2\pi N$ to $\hat{P} = 2\pi(N-1)$] is (assuming $N \gg 1$)

$$\Delta\tilde{E}_{B,ss} \simeq \frac{4\pi}{3\hat{P}}. \quad (31)$$

Thus $\Delta\tilde{E}_{B,\text{res}}/\Delta\tilde{E}_{B,ss} \sim 0.2|\Delta\hat{P}_1|^{1/3}$. In practice, systems that evolve into resonance rather than starting in resonance will reach a maximum mode energy of a few times Eq. 20, so $\Delta\tilde{E}_{B,\text{res}}$ can be comparable to $\Delta\tilde{E}_{B,ss}$.

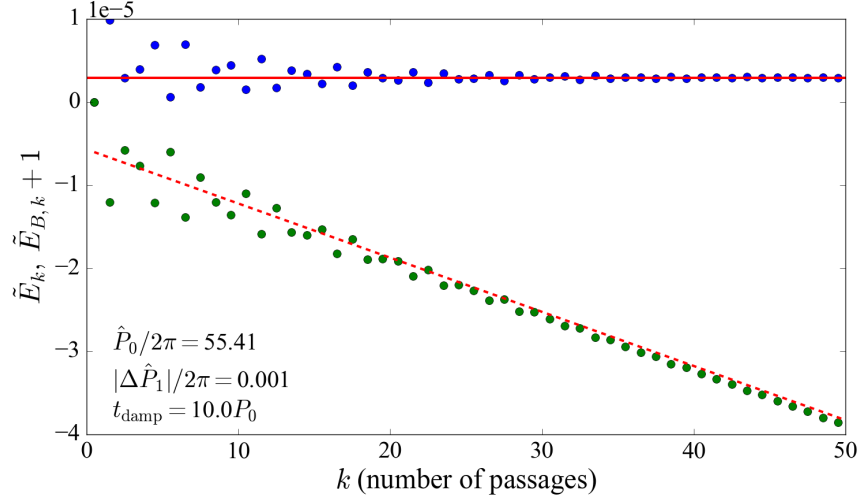


Figure 3: The stellar mode energy (blue dots) and the orbital energy (green dots; shifted for comparison) over 50 pericenter passages. Energy is normalized to the initial orbital energy of the binary. The solid red line shows the steady-state mode energy given by Eq. 29, and the dashed red line shows the orbital decay rate from Eq. 30.

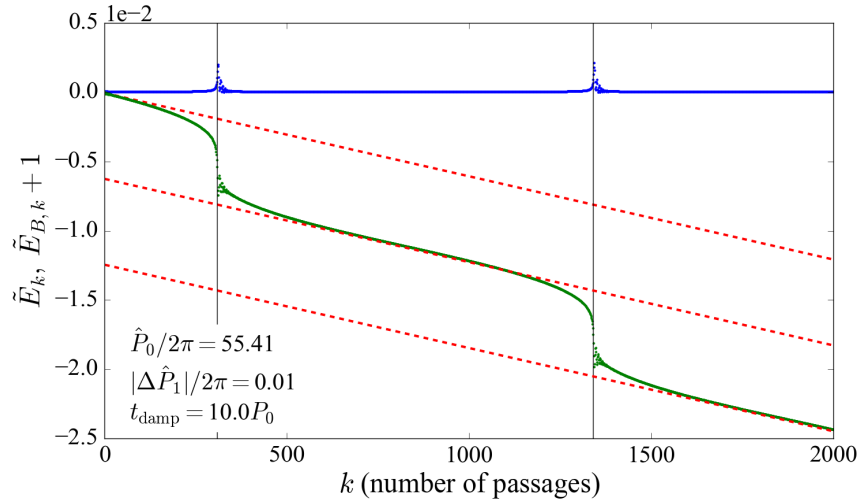


Figure 4: The mode energy (in blue) and the orbital energy (in green) over many pericenter passages. Energy is normalized to the initial orbital energy of the binary. The analytic orbital decay rate for the quasi-steady state is plotted in dashed red. The red lines are spaced by $5.46\tilde{E}_{\text{res}}$ with \tilde{E}_{res} given by Eq. 20.

Tamed Chaos In the presence of dissipation, even systems that experience chaotic mode growth eventually settle into a quasi-steady state. Figure 5 depicts an example. We see that initially the mode energy increases rapidly, accompanied by a large decrease in the orbital energy. For systems with relatively large damping rates, the mode energy may not reach the full “chaotic maximum” given by Eq. 25. However, for systems with relatively small damping rates, the full maximum energy is attainable. In either case, the mode energy ultimately decays to a quasi-steady value of order ΔE_1 after a timescale of $\sim t_{\text{damp}} \ln(E_{\text{max}}/\Delta E_1)$. The evolution of the system in quasi-steady state is well described by Eqs. 29-30.

We can understand how an initially chaotic system (with $|\Delta \hat{P}_1| \sim 1$) is brought into the “regular” regime by renormalizing various quantities to their “post-chaotic” values (see the lower panel of Fig. 5). Recall that the key parameter that determines the dynamical state of the system is $|\Delta \hat{P}| = \omega |\Delta P|$, with ΔP the change in the orbital period in a the first pericenter passage (i.e. when there is no prior oscillation). Since $|\Delta P|/P \simeq 3\Delta E/(2|E_B|)$ and ΔE is independent of the semi-major axis a (it depends only r_{peri} , which is almost unchanged), we find $|\Delta \hat{P}| \propto a^{5/2} \propto (1-e)^{-5/2}$ (for $r_{\text{peri}} = \text{constant}$; see Eq. 12). Thus, after significant orbital decay (with a decreased by a factor of a few), $|\Delta \hat{P}|$ is reduced to a “non-chaotic” value, and the system settles into the regular quasi-steady state.

We note that our model assumes linear mode damping. In reality, modes that are excited to high amplitudes may experience nonlinear damping. This will likely make the system evolve to the quasi-steady state more quickly. Other than this change of timescale, we expect that the various dynamical features revealed in our model remain valid. We note that a rapidly heated star/planet may undergo significant structural change depending on where heat is deposited. This may alter the frequencies of stellar modes. Our current model does not account for such feedback.

Systems with Multiple Modes Our analysis can be easily generalized to systems with multiple modes (labeled by the index α). The total energy in modes just before the $(k+1)$ -th passage is $\tilde{E}_k = \sum_{\alpha} |a_{\alpha,k}|^2$. During a pericenter passage, the amplitude of each mode changes by Δa_{α} . The total energy transferred to stellar modes in the k -th passage is

$$\Delta \tilde{E}_k = \sum_{\alpha} [|a_{\alpha,k-1} + \Delta a_{\alpha}|^2 - |a_{\alpha,k-1}|^2]. \quad (32)$$

As before, the orbital energy after the k -th passage is given by $\tilde{E}_{B,k} = \tilde{E}_{B,0} - \sum_{j=1}^k \Delta \tilde{E}_j$. The relationship between the orbital energy and the period is given by Eq. 4. The mode amplitude of each mode just before the $(k+1)$ -th passage is

$$a_{\alpha,k} = [a_{\alpha,k-1} + \Delta a_{\alpha}] e^{-(i+\hat{\gamma}_{\alpha})\hat{P}_{\alpha,k}} \quad (33)$$

where $\hat{P}_{\alpha,k} \equiv \omega_{\alpha} P_k$. Similarly, we define $|\Delta \hat{P}_{\alpha,1}| \equiv \omega_{\alpha} |\Delta P_1|$. The evolution of the system is completely determined by $\hat{P}_{\alpha,0}$, $|\Delta \hat{P}_{\alpha,1}|$ and $\hat{\gamma}_{\alpha} = \gamma_{\alpha}/\omega_{\alpha}$.

In general, systems with multiple modes exhibit the same types of behaviors seen in the single-mode system. Systems with small $|\Delta \hat{P}_{\alpha,1}|$ pass through multiple resonances over many orbits. For systems with many modes, resonances play a significant role in the orbital evolution. Multi-mode systems also exhibit chaotic growth that damps into a quasi-steady state. Appendix C provides a few samples of these types of behavior. Figure 6 shows two examples similar to

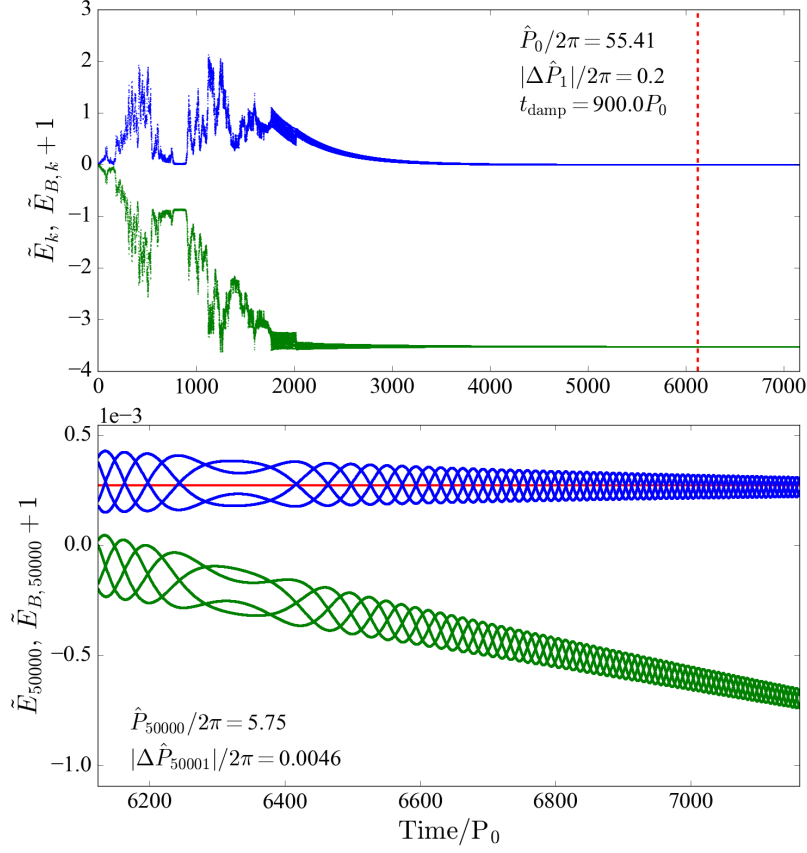


Figure 5: The mode energy (in blue) and the binary orbital energy (in green) over many peri-center passages. In the upper panel, the energy is normalized to the initial orbital energy of the binary. The mode energy undergoes chaotic evolution, and damps to a quasi-steady state after a few t_{damp} . The lower panel shows the later phase of the evolution (to the right of the dashed red line in the upper panel), with the energy re-normalized to the energy of the binary after 50,000 orbits. The predicted quasi-steady state mode energy is shown as a solid red line. The values of \hat{P} and $|\Delta\hat{P}|$ at 50,000 orbits are indicated. Note that because of the significant orbital decay during chaotic evolution, we use time (in units of P_0) rather than the number of orbits for the x -axis.

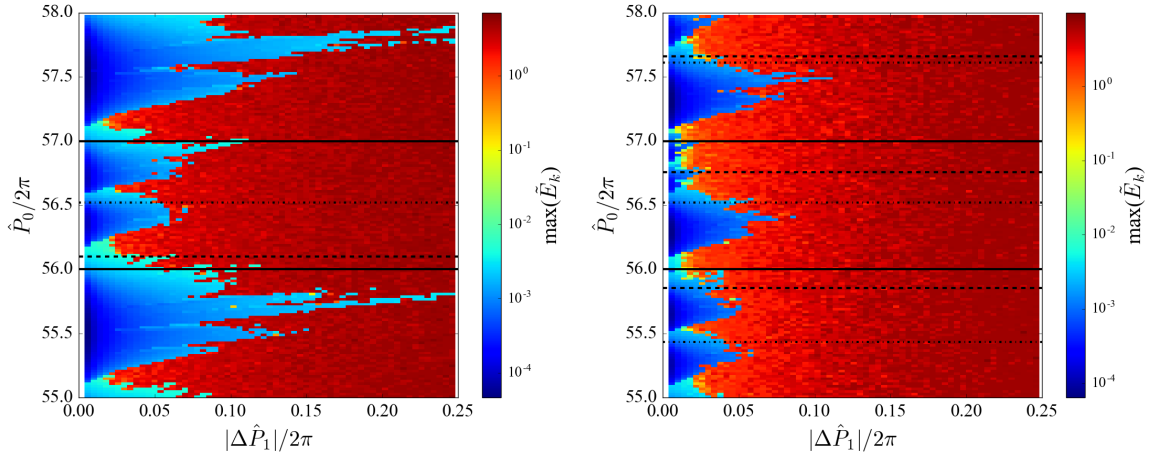


Figure 6: The maximum mode energy (summed over all modes) reached in 10,000 orbits as a function of $\omega_1|\Delta P_1|/2\pi$ and $\omega_1 P_0/2\pi$. In the dark blue regions, the modes exhibit low-energy oscillations, while in the dark red regions the modes grow chaotically to large amplitudes. The left panel shows a system with one dominant mode. The frequency ratios are $\omega_2/\omega_1 = 0.41$ and $\omega_3/\omega_1 = 0.46$. The energy ratios are $\Delta\tilde{E}_{2,1}/\Delta\tilde{E}_{1,1} = 0.04$ and $\Delta\tilde{E}_{3,1}/\Delta\tilde{E}_{1,1} = 0.03$. The dashed line corresponds to $\omega_2\hat{P}_0/2\pi = 23$, the dot-dashed line to $\omega_3\hat{P}_0/2\pi = 26$, and the solid lines to resonances for ω_1 . The right panel shows a system where all three modes are excited to similar energies. The frequency ratios are $\omega_2/\omega_1 = 1.11$ and $\omega_3/\omega_1 = 0.92$. The energy ratios are $\Delta\tilde{E}_{2,1}/\Delta\tilde{E}_{1,1} = 0.94$ and $\Delta\tilde{E}_{3,1}/\Delta\tilde{E}_{1,1} = 0.58$. The dashed lines corresponds to $\omega_2\hat{P}_0/2\pi = 62, 63, 64$, the dot-dashed lines to $\omega_3\hat{P}_0/2\pi = 51, 52, 53$, and the solid lines to resonances for ω_1 .

Fig. 1 that explore the parameter space of systems with three modes — one with a dominant mode, and another with (Δa_α) roughly equal for all modes. For application to stellar binaries, the example with a dominant mode is characteristic of a binary with $M \sim (\text{a few})M_\odot$ and a small pericenter separation ($\eta \sim 3$). For systems with larger η 's, the tidal potential tends to excite higher-order modes to similar amplitudes. Appendix D provides more detail on the choice of mode properties, which are determined using MESA stellar models and the non-adiabatic GYRE pulsation code (31, 32). In general, including multiple modes does not alter the classes of behaviors that the system exhibits. However, the multiple-mode model is more prone to chaotic evolution. Additionally, all modes, even those with relatively small Δa_α can guide the evolution of the system near resonance.

Summary and Discussion We have developed a mathematically simple, but physically accurate model for the evolution of eccentric binary systems driven by dynamical tides. The evolution of these systems can be described by an iterative map, and depends on three parameters — \hat{P}_0 , $|\Delta\hat{P}_1|$, and $\hat{\gamma}$, corresponding to the initial orbital period, the change in orbital period during the first pericenter passage, and the damping rate of an oscillation mode (see Eqs. 7-9). Multiple modes can be easily incorporated. For small $|\Delta\hat{P}_1|$, the mode exhibits low-amplitude oscillations that settle in to a quasi-steady state over a few mode damping times. When the mode

frequency is an integer multiple of the orbital frequency, the mode undergoes high-amplitude oscillations. As a system passes through a resonance, the orbital energy can decrease rapidly. For a system with large $|\Delta\dot{P}_1|$, the mode energy can undergo chaotic growth, rapidly shrinking and circularizing the orbit. After a few damping times, even chaotic systems settle into a quasi-steady state.

These results are applicable to a variety of astrophysical systems mentioned in the introduction. In particular, a tidally captured star around a compact object in dense clusters or a massive black hole at the center of galaxies may experience chaotic growth of mode amplitude during multiple pericenter passages, accompanied by significant orbital decay and tidal heating. A similar evolution may occur when a giant planet (“cold Jupiter”) is excited into a high-eccentricity orbit by an external companion (a distant star or a nearby planet) via the Lidov-Kozai mechanism (10–15). We have found that a $m_p \sim 1 M_J$ planet pushed into an orbit with pericenter distance $\lesssim 0.015$ AU and $e \gtrsim 0.95$ will enter the chaotic regime for the growth of f-modes. The planet can spend an appreciable time in the high- e phase of the Lidov-Kozai cycle, allowing the mode energy to reach the maximum value ($E_{\alpha,\max} \sim \text{a few} \times GM_\star m_p/a$). Such modes are highly nonlinear [$E_{\alpha,\max}/(Gm_p^2/R_p) \sim 1$ for $a \sim 1$ AU], and will suffer rapid nonlinear decay. The consequence is that the planet’s orbit rapidly shrinks (by a factor of a few), similar to the behavior depicted in Fig. 5, and the system eventually enters a quasi-steady state with slow orbital decay. We suggest that this is a promising mechanism for forming warm Jupiters, whose origin remains poorly understood (33–36).

Our study has revealed a rich variety of dynamical behaviors for highly eccentric binaries undergoing tidal interactions. Nevertheless, our model is still idealized. One effect we did not include is stellar (or planetary) rotation. The qualitative behaviors of systems that undergo low-amplitude oscillations or chaotic evolution are unlikely to change with the inclusion of rotation. However, tidal spin-up of the star (and tidal heating) can directly affect the mode frequencies, giving rise to the possibility of resonance locking under some conditions, which may extend the time frame over which the orbital energy rapidly decreases (20–22, 37). In addition, as noted above, our assumption of linear damping may fail in the chaotic regime; non-linear damping could lead to even more rapid orbital evolution and significant structural changes in the excited star or planet. All of these issues deserve further study.

Acknowledgements: This work has been supported in part by NASA grants NNX14AP31G and NNX14AG94G, and a Simons Fellowship in theoretical physics (DL). MV is supported by a NASA Earth and Space Sciences Fellowship in Astrophysics. DL thanks the hospitality of the Institute for Advanced Study (Fall 2016) where this work started.

References

1. A. C. Fabian, J. E. Pringle, M. J. Rees, *MNRAS* **152**, 15 (1975).
2. W. H. Press, S. A. Teukolsky, *ApJ* **213**, 183 (1977).
3. H. M. Lee, J. P. Ostriker, *ApJ* **310**, 176 (1986).
4. N. C. Stone, A. H. W. Küpper, J. P. Ostriker, *MNRAS* **467**, 4180 (2017).
5. M. J. Rees, *Nature* **333**, 523 (1988).
6. N. C. Stone, B. D. Metzger, *MNRAS* **455**, 859 (2016).

7. J. Guillochon, (<https://tde.space/>).
8. M. Vick, D. Lai, J. Fuller, *MNRAS* **468**, 2296 (2017).
9. M. MacLeod, J. Goldstein, E. Ramirez-Ruiz, J. Guillochon, J. Samsing, *ApJ* **794**, 9 (2014).
10. Y. Wu, N. Murray, *ApJ* **589**, 605 (2003).
11. D. Fabrycky, S. Tremaine, *ApJ* **669**, 1298 (2007).
12. M. Nagasawa, S. Ida, T. Bessho, *ApJ* **678**, 498 (2008).
13. C. Petrovich, *ApJ* **799**, 27 (2015).
14. K. R. Anderson, N. I. Storch, D. Lai, *MNRAS* **456**, 3671 (2016).
15. D. J. Muñoz, D. Lai, B. Liu, *MNRAS* **460**, 1086 (2016).
16. S. E. Thompson, *et al.*, *ApJ* **753**, 12 (2012).
17. P. G. Beck, *et al.*, *A&A* **564**, 18 (2014).
18. B. Kirk, *et al.*, *AJ* **151**, 21 (2016).
19. W. F. Welsh, *et al.*, *ApJ* **197**, 4 (2011).
20. J. Fuller, D. Lai, *MNRAS* **420**, 3126 (2012).
21. J. Burkart, *et al.*, *MNRAS* **421**, 983 (2012).
22. J. Fuller, *submitted MNRAS* (2017).
23. R. A. Mardling, *ApJ* **450**, 722 (1995).
24. P. B. Ivanov, J. C. B. Papaloizou, *MNRAS* **347**, 437 (2004).
25. R. A. Mardling, *ApJ* **450**, 732 (1995).
26. P. Kumar, J. Goodman, *ApJ* **466**, 946 (1996).
27. D. Lai, *ApJ* **466**, L35 (1996).
28. D. Lai, *ApJ* **490**, 847 (1997).
29. P. B. Ivanov, J. C. B. Papaloizou, *Celestial Mechanics and Dynamical Astronomy* **111**, 51 (2011).
30. J. G. Hills, *Nature* **254**, 295 (1975).
31. B. Paxton, L. Bildsten, A. Dotter, F. Herwig, P. Lesaffre, F. Timmes, *ApJ* **192**, 3 (2011).
32. R. H. D. Townsend, S. A. Teitler, *MNRAS* **435** 3406 (2013).
33. C. Petrovich, S. Tremaine, *ApJ* **829**, 20 (2016).

34. F. Antonini, A. S. Hamers, Y. Lithwick, *AJ* **152**, 15 (2016).
35. C. Huang, Y. Wu, A. H. M. J. Triaud, *ApJ* **825**, 10 (2016).
36. K. R. Anderson, D. Lai, in press (available at <https://arxiv.org/pdf/1706.00084.pdf>).
37. M. G. Witte, G. J. Savonije, *A&A* **350**, 129 (1999).
38. A. K. Schenk, *et al.*, *Phys. Rev. D* **65**, 2 (2002).
39. D. Lai, Y. Wu, *Phys. Rev. D* **74**, 2 (2006).

A Physical Justification for the Iterative Map

We present a brief derivation of the iterative map based on the hydrodynamics of forced stellar oscillations in binaries. We consider the tidally-excited oscillations of the primary body (mass M and radius R) by the companion of mass M' . The gravitational potential produced by M' reads

$$U(\mathbf{r}, t) = -GM' \sum_{lm} \frac{W_{lm} r^l}{D^{l+1}} e^{-im\Phi(t)} Y_{lm}(\theta, \phi), \quad (34)$$

where $\mathbf{r} = (r, \theta, \phi)$ is the position vector (in spherical coordinates) relative to the center of mass of M , $D(t)$ is the binary separation and Φ is the orbital true anomaly. The dominant quadrupole terms have $l = |m| = 2$ and $m = 0$, for which $W_{2\pm 2} = (3\pi/10)^{1/2}$ and $W_{20} = (\pi/5)^{1/2}$. For simplicity, we neglect stellar rotation [see (38, 39)]. To linear order, the response of star M to the tidal forcing frequency is specified by the Lagrangian displacement $\boldsymbol{\xi}(\mathbf{r}, t)$. A free oscillation mode of frequency ω_α has the form $\boldsymbol{\xi}_\alpha(\mathbf{r}, t) = \boldsymbol{\xi}_\alpha(\mathbf{r}) e^{-i\omega_\alpha t} \propto e^{im\phi - i\omega_\alpha t}$. We carry out phase-space expansion of $\boldsymbol{\xi}(\mathbf{r}, t)$ in terms of the eigenmodes (38):

$$\begin{bmatrix} \boldsymbol{\xi} \\ \partial \boldsymbol{\xi} / \partial t \end{bmatrix} = \sum_{\alpha} c_{\alpha}(t) \begin{bmatrix} \boldsymbol{\xi}_{\alpha}(\mathbf{r}) \\ -i\omega_{\alpha} \boldsymbol{\xi}_{\alpha}(\mathbf{r}) \end{bmatrix}. \quad (35)$$

The linear fluid dynamics equations for the forced stellar oscillations then reduce to the evolution equation for the mode amplitude $c_{\alpha}(t)$ (39):

$$\dot{c}_{\alpha} + (i\omega_{\alpha} + \gamma_{\alpha})c_{\alpha} = \frac{iGM'W_{lm}Q_{\alpha}}{2\omega_{\alpha}D^{l+1}} e^{-im\Phi(t)}, \quad (36)$$

where γ_{α} is the mode (amplitude) damping rate, $Q_{\alpha} = \int d^3x \rho \boldsymbol{\xi}_{\alpha}^* \cdot \nabla(r^l Y_{lm})$ is the tidal overlap integral, and the eigenmode is normalized according to $\int d^3x \rho(\mathbf{r}) |\boldsymbol{\xi}_{\alpha}(\mathbf{r})|^2 = 1$.

The general solution to Eq. 36 is

$$c_{\alpha} = e^{-(i\omega_{\alpha} + \gamma_{\alpha})t} \int_{t_0}^t \frac{iGM'W_{lm}Q_{\alpha}}{2\omega_{\alpha}D^{l+1}} e^{(i\omega_{\alpha} + \gamma_{\alpha})t' - im\Phi(t')} dt'. \quad (37)$$

For eccentric binaries, we can write this as a sum over multiple pericenter passages. To do so, let t_k be the time of the k -th apocentre passage. [Note that, for the moment, this use of k

differs from the meaning used in Eqs. 1-5, where it is used to describe the number of pericenter passages]. We can relate t_k to t_{k-1} via

$$t_k = t_{k-1} + \frac{1}{2}(P_{k-1} + P_k). \quad (38)$$

Now define

$$\Delta c_\alpha = \int_{-P_{k-1}/2}^{P_k/2} \frac{iGM'W_{lm}Q_\alpha}{2\omega_\alpha D^{l+1}} e^{(i\omega_\alpha + \gamma_\alpha)t' - im\Phi(t')} dt'. \quad (39)$$

This is the change in mode amplitude during a pericenter passage, and it is approximately constant for any k provided the orbit is very eccentric and the pericenter distance r_{peri} remains constant (see the main text for discussion). We can then write c_α at time t_k simply as

$$c_{\alpha,k} = e^{-(i\omega_\alpha + \gamma_\alpha)t_k} \Delta c_\alpha \sum_{j=1}^k e^{(i\omega_\alpha + \gamma_\alpha)(t_{j-1} + P_{j-1}/2)}. \quad (40)$$

We can reorganize Eq. 40 into an iterative form

$$c_{\alpha,k} = c_{\alpha,k-1} e^{-(i\omega_\alpha + \gamma_\alpha)(P_{k-1} + P_k)/2} + e^{-(i\omega_\alpha + \gamma_\alpha)P_k/2} \Delta c_\alpha. \quad (41)$$

We now shift the index k to count pericenter passages rather than apocentre passages by defining $a_{\alpha,k} = c_{\alpha,k} e^{-i\omega P_k/2}$ to recover

$$a_{\alpha,k} = (a_{\alpha,k-1} + \Delta a_\alpha) e^{-(i\omega_\alpha + \gamma_\alpha)P_k}, \quad (42)$$

where $\Delta a_\alpha = \Delta c_\alpha$.

B Non-dissipative Systems

B.1 Maximum Mode Energy for Non-Chaotic Systems

In the oscillatory and resonant regimes, the mode energy $\tilde{E}_k \ll 1$, and the iterative map given by Eq. 19 can be rewritten:

$$z_{k+1} \simeq 1 + z_k e^{-i\hat{P}_0 + i|\Delta\hat{P}_1||z_k|^2}, \quad (43)$$

where $z_k \equiv a_{k-}/\Delta a = a_{k-1}/\Delta a + 1$.

Oscillatory Regime: When $|\delta\hat{P}_0| = |\hat{P}_0 - 2\pi N| \gg |\Delta\hat{P}_1||z_k|^2$, the map simplifies to

$$z_{k+1} \simeq 1 + z_k e^{-i\hat{P}_0}. \quad (44)$$

This yields the solution (for $z_1 = 1$)

$$z_k \simeq \frac{1 - e^{-ik\hat{P}_0}}{1 - e^{-i\hat{P}_0}}, \quad (45)$$

which is equivalent to Eq. 16. The validity of this oscillatory solution requires $|\delta\hat{P}_0| \gg |\Delta\hat{P}_1|/(1 - \cos\hat{P}_0)$ or $|\delta\hat{P}_0|^3 \gg |\Delta\hat{P}_1|$.

Resonant Regime: When $|\delta\hat{P}_0|^3 \ll |\Delta\hat{P}_1|$, the system is in the resonant regime, and the map becomes

$$z_{k+1} - z_k \simeq 1 + i|\Delta\hat{P}_1||z_k|^2 z_k. \quad (46)$$

For $k \gg 1$, we can approximate the mode amplitude as a continuous function of k , and the above equation reduces to

$$\frac{dz}{dk} \simeq 1 + i|\Delta\hat{P}_1||z|^2 z. \quad (47)$$

Now we express z explicitly in terms of an amplitude A and phase θ :

$$z = A e^{i\theta}. \quad (48)$$

Equation (47) can be rewritten as two differential equations:

$$\frac{dA}{dk} \simeq \cos\theta, \quad (49)$$

$$\frac{d\theta}{dk} \simeq \frac{1}{A} \left(|\Delta\hat{P}_1| A^3 - \sin\theta \right). \quad (50)$$

We combine these to examine how the amplitude varies with the phase:

$$\frac{dA}{d\theta} = \frac{A \cos\theta}{\left(|\Delta\hat{P}_1| A^3 - \sin\theta \right)}. \quad (51)$$

To solve the above equation, we use the substitutions

$$u = |\Delta\hat{P}_1| A^3, \quad v = \sin\theta. \quad (52)$$

Eq. 51 then simplifies to

$$\frac{du}{dv} = \frac{3u}{u - v}. \quad (53)$$

For the initial condition $u = v = 0$, which corresponds to $a_0 = 0$, the solution is simply $u = 4v$, or

$$A = \left(\frac{4 \sin\theta}{|\Delta\hat{P}_1|} \right)^{1/3}, \quad (54)$$

which has the maximum value $(4/|\Delta\hat{P}_1|)^{1/3}$. The maximum mode energy for a system near resonance is therefore

$$\tilde{E}_{\text{res}} \equiv \tilde{E}_{k,\text{max}} = (\Delta a)^2 \left(\frac{4}{|\Delta\hat{P}_1|} \right)^{2/3} \simeq \frac{2^{7/3}}{3} \frac{|\Delta\hat{P}_1|^{1/3}}{\hat{P}_0}. \quad (55)$$

We can use the above result to approximate the shape that the mode amplitude traces in the complex plane over many orbits. Our numerical calculation (see Fig. 2) shows that the mode amplitude as a function of its phase can be described by

$$\left| \frac{a_k}{\Delta a} + 0.5 \right| \simeq \left(\frac{4 \sin \theta}{|\Delta \hat{P}_1|} \right)^{1/3}, \quad (56)$$

where θ is the phase of $a_k/\Delta a + 0.5$. This is similar to Eq. 54 except for a shift along the real axis. For $|\Delta \hat{P}_1| \ll 1$, this approximation performs very well, as seen in Fig. 2.

B.2 Resonant Timescale

The mode of a non-dissipative system near resonance evolves periodically, repeatedly tracing out a closed shape in the complex amplitude plane. We define t_{res} as the period of the resonant oscillations. To calculate this timescale, we use Eqs. 49 and 54 to find

$$\frac{d\theta}{dk} \simeq \left(\frac{|\Delta \hat{P}_1|}{4} \right)^{1/3} 3(\sin \theta)^{2/3}. \quad (57)$$

Integrating the above differential equation from $\theta = 0$ to $\theta = \pi$ gives

$$t_{\text{res}} \simeq 3.85 P |\Delta \hat{P}_1|^{-1/3}, \quad (58)$$

where P is the orbital period associated with the resonance. In order of magnitude, the number of orbits necessary to reach the maximum mode amplitude $|a_{\text{res}}| \sim |\Delta \hat{P}_1|^{-1/3} \Delta a$ is simply $|a_{\text{res}}|/\Delta a$.

B.3 Lyapunov Exponent for Chaotic Systems

We can verify that the dynamical behavior of systems with a large $|\Delta \hat{P}_1|$ is chaotic by examining the difference between a trajectory and its shadow to estimate the Lyapunov exponent. The shadow trajectory is calculated with a slightly different initial value $a_{0,\text{shadow}}$, such that $\delta a_0 \equiv |a_{0,\text{shadow}}| - |a_0| \ll 1$. We follow the evolution of $\delta a_k \equiv ||a_{k,\text{shadow}}| - |a_k||$. For chaotic behavior, we expect

$$\delta a_k \approx \delta a_0 e^{\lambda k}, \quad (59)$$

where λ is the Lyapunov exponent.

Figure 7 suggests that systems with $|\Delta \hat{P}_1| \sim 1$ indeed undergo chaotic evolution, with δa_k growing exponentially (but eventually saturating when $\delta a_k \sim 0.1$). For the system depicted in Fig. 7, $\lambda \approx 1.77$. The exact value of λ can change slightly with the parameters \hat{P}_0 and $|\Delta \hat{P}_1|$.

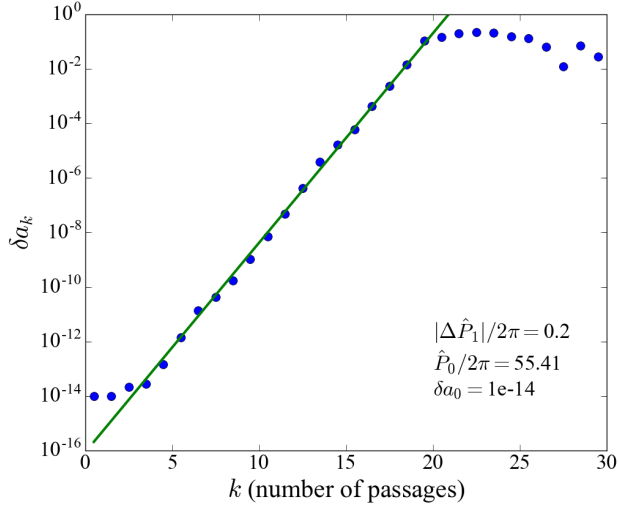


Figure 7: The blue dots show the difference between the mode amplitude of a trajectory and its shadow, δa_k , as a function of orbits. The green line shows a fit to the exponential rise with $\lambda \approx 1.77$, where λ is defined in Eq. 59). For $k \gtrsim 20$, δa_k saturates around 0.1.

B.4 Maximum Mode Energy for Chaotic Systems

As discussed in the main text, the mode energy of a chaotic system initially grows stochastically with an expected value of $\langle \tilde{E}_k \rangle \sim \Delta \tilde{E}_1 k$ (see Eq. 23 and Fig. 8), but cannot exceed a maximum value, \tilde{E}_{\max} . As the mode energy increases, the change in the orbital period between pericenter passages, $\Delta \hat{P}_k$, decreases (see Eq. 24). The maximum mode energy is approximately set by $|\Delta \hat{P}_k| \sim 1$, and is given by Eq. 25.

In reality, the dependence of \tilde{E}_{\max} on \hat{P}_0 and $|\Delta \hat{P}_1|$ is more complicated than the power law trend from Eq. 25. Figures 9 and 10 show “jumps” and “drops” in \tilde{E}_{\max} at some values of \hat{P}_0 and $|\Delta \hat{P}_1|$. To understand this step-like behavior, we note that the maximum mode energy for a non-dissipative system is associated with the minimum (dimensionless) orbital period by

$$\hat{P}_{\min} = \hat{P}_0 \left(\frac{1}{1 + \tilde{E}_{\max}} \right)^{3/2}. \quad (60)$$

We have found that for a chaotic system, as $|\Delta \hat{P}_k|$ decreases toward unity, the orbital period tends to evolve away from resonances with the stellar mode and to linger directly between them. This behavior can be understood from the fact that, for a system near resonance, the shifts in mode amplitude during pericenter tend to add over successive passages, pushing the system away from the resonance. Imposing $\hat{P}_{\min} \simeq 2\pi(N + 1/2)$ yields

$$\tilde{E}_{\max} \simeq \left[\frac{\hat{P}_0}{2\pi(N + 1/2)} \right]^{2/3} - 1. \quad (61)$$

Eq. 61 is in good agreement with results shown in Figs. 9 and 10. We see that the jumps in \tilde{E}_{\max} correspond to changes in N . Combining Eq. 61 with the broader trend of Eq. 25 captures the main features of how \tilde{E}_{\max} depends on \hat{P}_0 and $|\Delta\hat{P}_1|$ for chaotic systems.

C Multiple Modes

When multiple modes are included in the model, we see the same types of behaviors as for the single-mode model. For systems with small $|\Delta\hat{P}_1|$, as the mode energy is dissipated, the shrinking orbit can pass through resonances with multiple modes. Figure 11 shows an example of this behavior. Systems that initially exhibit chaotic behavior still damp to a quasi-steady state when multiple modes are included, as shown in Fig. 12.

D G-mode Properties of Stellar Models

One application of our model is the tidal capture of main-sequence stars by compact objects, including massive black holes. We use the stellar evolution code, MESA (31), and the non-adiabatic pulsation code, GYRE (32), to determine the properties of g-modes in the radiative envelope of stars between 2 and $10M_{\odot}$. The characteristic damping times of modes are found using the imaginative part of the mode frequency. These values are generally in good agreement with a quasi-adiabatic approximation that assumes radiative damping. Figure 13 shows the computed damping rates for three stellar models. For the $2M_{\odot}$ model, the damping rate only varies by a factor of a few for the relevant g-modes. For the $10M_{\odot}$ model (and other models with $10M_{\odot} \leq M \leq 20M_{\odot}$), the damping rates are much smaller for higher frequency modes.

The amount of energy transferred to a mode (labelled α) in the “first” pericenter passage $\Delta E_{\alpha,1}$ (i.e., when the oscillation amplitude is zero before the passage) depends on the stellar structure and mode properties. We use the method of Ref. (2) to calculate $\Delta E_{\alpha,1}$. The quasi-steady-state mode dissipation rate from Eq. 29 is of order $\gamma_{\alpha}\Delta E_{\alpha,1}$. Figure 14 shows an example of the calculated $\Delta E_{\alpha,1}$ and the energy dissipation rates for systems with different stellar properties and $\eta = 3$. We find that stars with $M \lesssim 5M_{\odot}$ tend to have a single low-order g-mode with large $\Delta\tilde{E}_{\alpha,1}$ that dominates the energy transfer rate. To represent a system with a dominant mode, we choose the ω and γ ratios between modes from the $2M_{\odot}$ model and the $\tilde{E}_{\alpha,1}$ ratio for $\eta = 3$. More massive stars ($M \gtrsim M_{\odot}$) have a number of g-modes that contribute roughly equally to the energy transfer rate. To represent a system where multiple modes are important for energy transfer, we choose the ω and γ ratios between modes from the $10M_{\odot}$ model and the $\tilde{E}_{\alpha,1}$ ratio for $\eta = 3$.

The orbital parameter $\eta = (r_{\text{peri}}/R)(M/M_t)^{1/3}$ (where r_{peri} is the pericenter distance) also strongly affects $\Delta E_{\alpha,1}$, though the dependence on e is negligible for highly eccentric orbits. For larger η , the orbital frequency at pericenter is smaller, and higher-order g-modes contribute more to tidal energy transfer, as illustrated in Fig. 15.

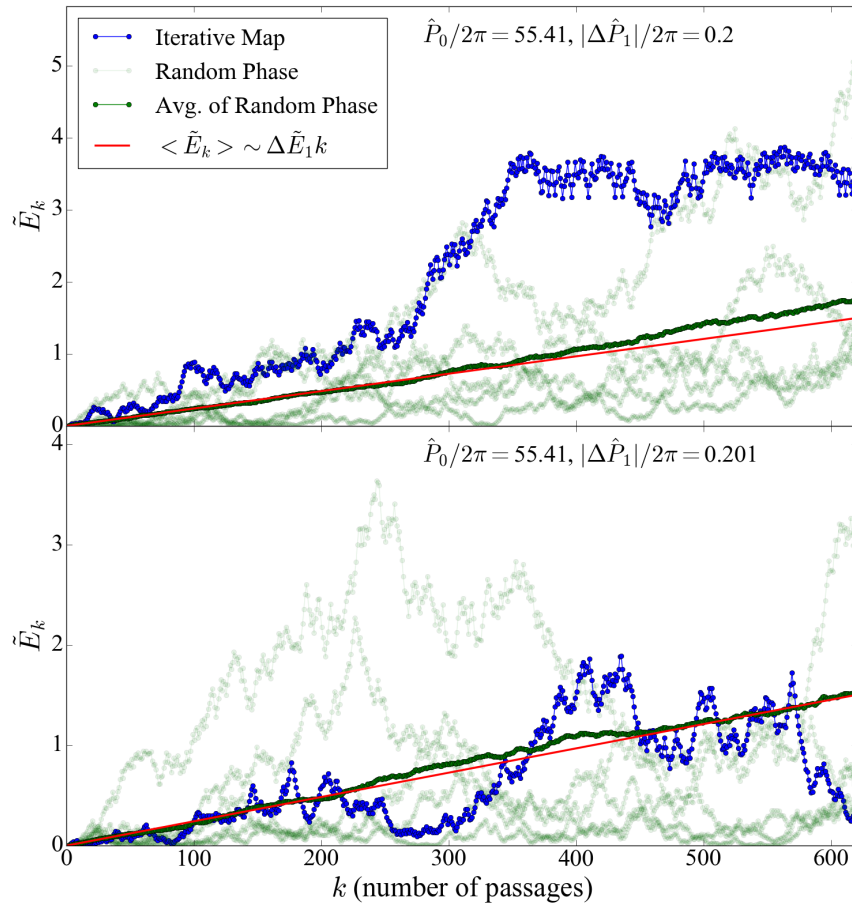


Figure 8: The mode energy evolution for two slightly different values of $|\Delta\hat{P}_1|$. The blue lines are the results from the iterative map; the light green lines show examples of the random phase model [where \hat{P}_k in Eq. 21 takes on random values between 0 and 2π]; the dark green is an average of 100 iterations of the random phase model; and the red lines show the expected average growth of the mode energy in the diffusion model.

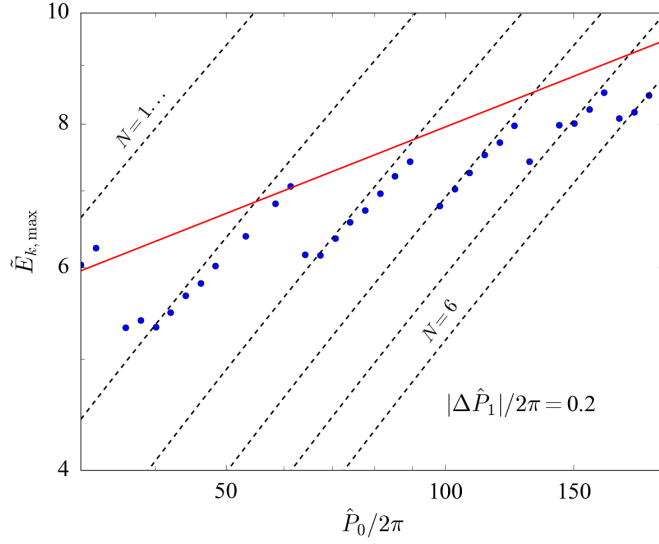


Figure 9: Numerical results for \tilde{E}_{\max} (blue dots) after 3×10^6 orbits for chaotic systems with $|\Delta\hat{P}_1|/2\pi = 0.2$. The red line is $1.5(\hat{P}_0|\Delta\hat{P}_1|)^{1/4}$ (see Eq. 25). The dotted lines are from Eq. 61 with different values of N .

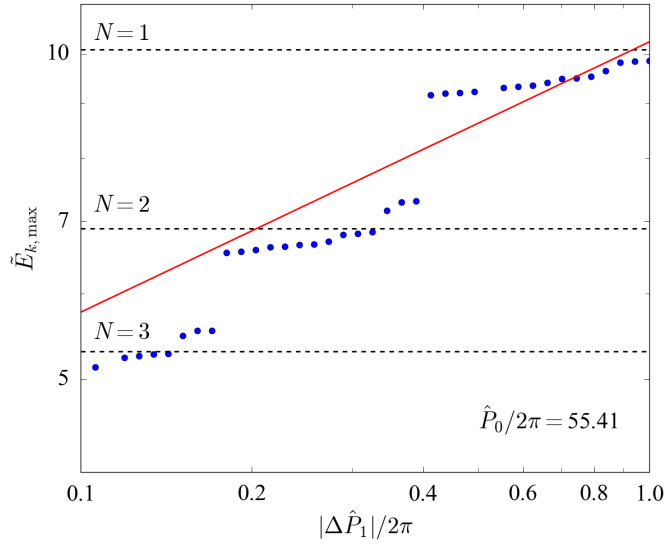


Figure 10: Numerical results for \tilde{E}_{\max} (blue dots) after 3×10^6 orbits for chaotic systems with $\hat{P}_0/2\pi = 55.41$. The red line is $1.5(\hat{P}_0|\Delta\hat{P}_1|)^{1/4}$ (see Eq. 25). The dotted lines are from Eq. 61 with different values of N .

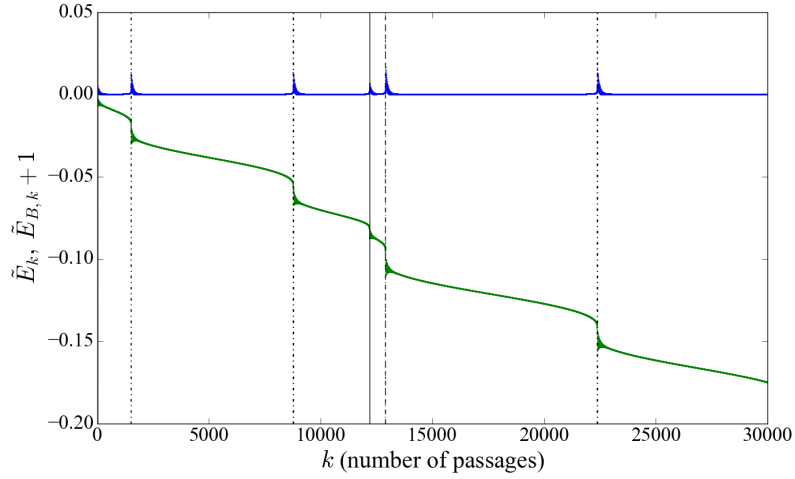


Figure 11: The total mode energy and orbital energy of a system with three modes that evolves through multiple resonances. The properties of the modes are discussed in detail in Appendix D. For this system, the parameters are $\hat{P}_{\alpha,0}/2\pi = 123, 56.6, 50.4$ and $|\Delta\hat{P}_{\alpha,1}|/2\pi = 0.1, 0.05, 0.04$. The mode damping times are all of order $t_{\text{damp}} \sim 100P_0$. Resonances for different modes are shown with vertical solid, dashed, and dot-dashed lines.

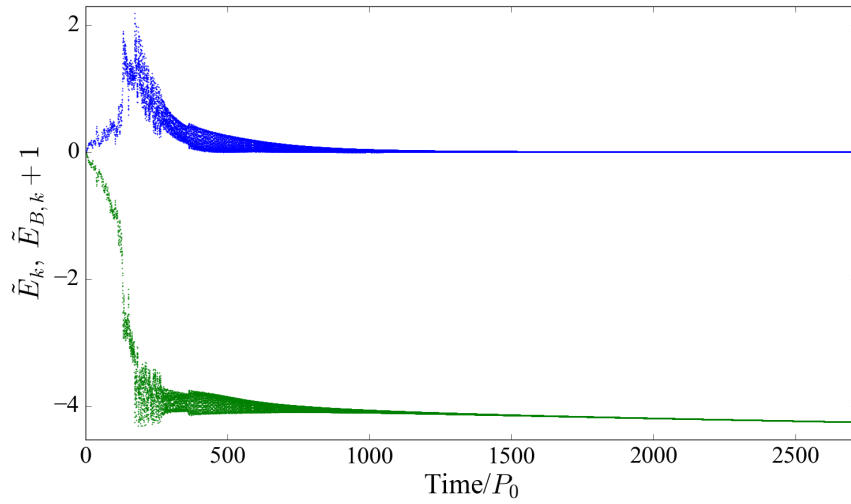


Figure 12: The total mode energy and orbital energy of a system with three modes that undergoes initial chaotic growth and eventually damps to a quasi-steady state. The properties of the modes are discussed in detail in Appendix D. For this system, the parameters are $\hat{P}_{\alpha,0}/2\pi = 123, 137, 113$ and $|\Delta\hat{P}_{\alpha,1}|/2\pi = 2.3, 2.5, 2.1$. The mode damping times are all of order $t_{\text{damp}} \sim 100P_0$.

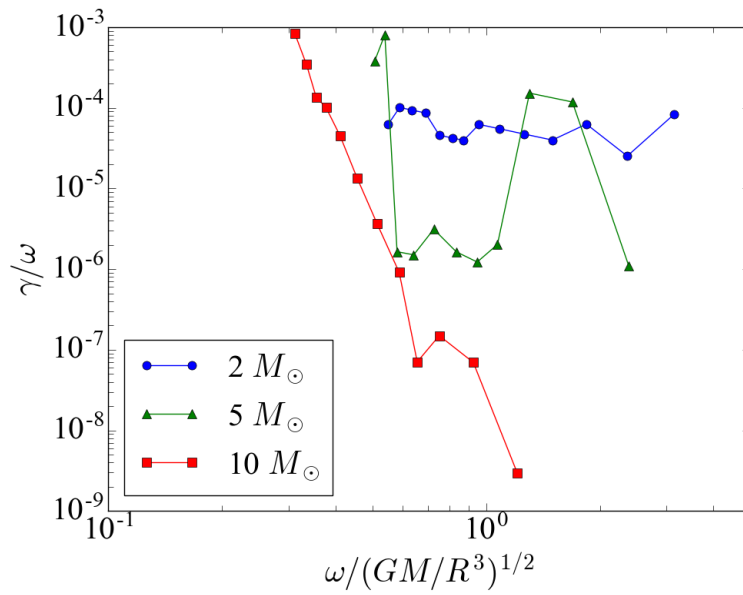


Figure 13: Numerical results for the g-mode frequencies (ω) and damping rates (γ) of three MESA stellar models analysed with the non-adiabatic stellar pulsation code, GYRE. The dip in γ/ω for the $5M_\odot$ model is typical for models in the mass range $4 - 8M_\odot$.

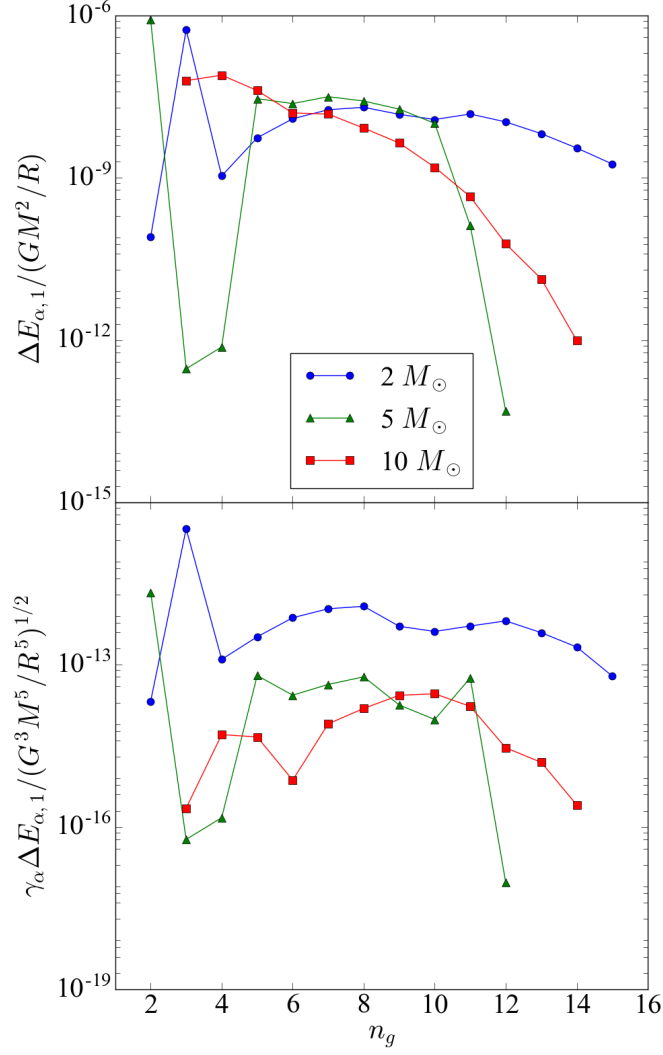


Figure 14: Numerical results for $\Delta E_{\alpha,1}$ and $\gamma_\alpha \Delta E_{\alpha,1}$ vs. n_g (the radial mode number) for three MESA stellar models analysed with the non-adiabatic stellar pulsation code, GYRE. The energy transfer $\Delta E_{\alpha,1}$ is calculated assuming $\eta = 3$ and $e = 0.95$.

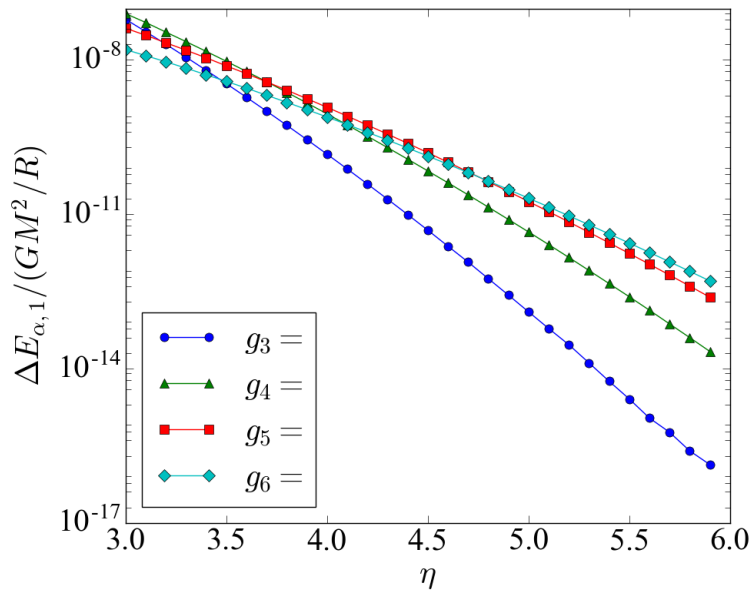


Figure 15: Numerical results for $\Delta E_{\alpha,1}$ for four g-modes of the $10M_{\odot}$ stellar model as a function of η . For larger η , higher order g-modes receive more energy at pericenter than lower-order g-modes.